Nano Energy 27 (2016) 95–102

Contents lists available at ScienceDirect

Nano Energy

journal homepage: www.elsevier.com/locate/nanoen

# *In-situ* TEM experiments and first-principles studies on the electrochemical and mechanical behaviors of α-$MoO_3$ in Li-ion batteries

Yonghe Li [a], Hong Sun [b], Xiaopeng Cheng [a], Yuefei Zhang [a,*], Kejie Zhao [b,*]

[a] Institute of Microstructure and Property of Advanced Materials, Beijing University of Technology, Beijing 100124, PR China
[b] School of Mechanical Engineering, Purdue University, West Lafayette, IN 47906, USA

ARTICLE INFO

*Article history:*
Received 29 April 2016
Received in revised form
21 June 2016
Accepted 23 June 2016
Available online 29 June 2016

*Keywords:*
Metal oxides
$MoO_3$
High capacity
Cracks
Li-ion batteries

ABSTRACT

Metal oxides hold the promise of high-capacity anodes for Li-ion batteries. Lithiation of binary metal oxides proceeds with two typical mechanisms: insertion and conversion. We characterize the two-step lithiation behavior of α-$MoO_3$, namely, Li intercalation in the layered α-$MoO_3$ leads to the formation of crystalline $Li_2MoO_3$ in the early stage of lithiation, and further Li insertion coverts $Li_xMoO_3$ to metallic Mo and amorphous $Li_2O$. The intercalation process is thermodynamically more favorable and is accompanied with a minor volumetric change, while the conversion reaction is kinetically slow and induces large deformation. Furthermore, instead of showing significant Li-embrittlement as seen in typical oxides, α-$MoO_3$ remains defects free despite the nearly 100% repetitive volumetric change during lithiation cycles. The reaction mechanism, structural evolution, and mechanical behaviors are unveiled through co-ordinated *in-situ* transmission electron microcopy experiments on α-$MoO_3$ nanobelts and first-principles computational studies. The results provide fundamental perspectives in the course of developing reliable high-capacity electrodes for Li-ion batteries.



## 1. Introduction

Li-ion batteries are the state-of-the-art choice in portable electronics, electric vehicles, and electric energy storage system [1,2]. Technological improvement in rechargeable batteries has been driven by the ever-increasing demand on electrodes of high energy density and superior electrochemical and mechanical stabilities [3]. As an alternative to graphite, metal oxides hold the great promise of high-capacity anodes given the wealth of compounds of various degrees of covalence and metal oxidation states that enable the tuning of equilibrium potential and charging kinetics for Li-ion batteries [4,5].

Lithiation of metal oxides proceeds with the co-absorption of Li ions and electrons. The metal ions serve as the redox center for the electron injection. The Li storage in the host metal oxides is under two typical mechanisms: insertion and conversion. The respective lithiation mechanism shows a rough correlation with the atomic number of the 3*d* transition metal oxides [5]. This feature was understood based on the thermodynamic driving force of lithiation reaction and the kinetic factor of M–O bond dissociation. For the early transition metal oxides, the equilibrium potential *vs.* $Li/Li^+$ of conversion reaction is low. Meanwhile, the metal ions are more polarized and the dissociation energy of M–O bonds is stronger in the early transition metal oxides than that of the later compounds. Therefore, conversion reaction is generally more favorable for the later transition metal oxides. For the insertion-type oxides, such as $TiO_2$ and $V_2O_5$ [6–9], Li is absorbed at well-defined interstitial sites in the form of one-dimensional channels and two-dimensional van der Waals layers in crystalline structures or at structural defects populated in amorphous lattice. The capacity of insertion-type metal oxides is limited by the available sites for Li occupation. Nevertheless, one noticeable merit is that Li insertion and extraction do not significantly distort the host structure and thus the mechanical stability can be retained in the long-term cycles. For the conversion-type materials, such as $Co_3O_4$, CuO, $Fe_2O_3$, and NiO [9–15]. the injection of Li ions and electrons translates the metal oxides into the elemental metal and lithium oxides through the following reaction: $M_aO_b + (b \cdot n)\,Li \leftrightarrow aM + bLi_nO$. In general, the conversion-type metal oxides preserve higher capacity (typical theoretical capacity $\sim$1000 mA h $g^{-1}$) than the insertion-type materials. However, the long-term cyclability may be compromised by the mechanical

* Corresponding authors.
*E-mail addresses:* yfzhang@bjut.edu.cn (Y. Zhang), kjzhao@purdue.edu (K. Zhao).

http://dx.doi.org/10.1016/j.nanoen.2016.06.045
2211-2855/

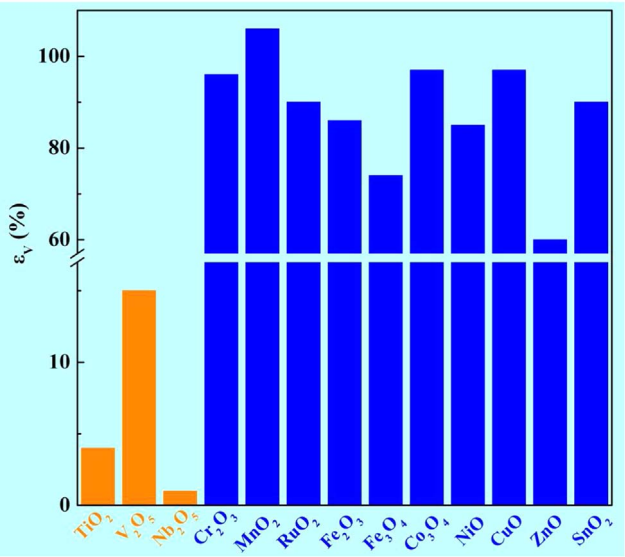


**Fig. 1.** A brief overview of the theoretical volumetric strains in binary metal oxides. The orange color represents the insertion-type oxides, and the blue color represents the conversion-type materials.

instability and structural disintegration induced by repetitive large volumetric change during lithiation cycles. Fig. 1 provides an overview of the volumetric strain for the insertion- and conversion-type binary metal oxides. The theoretical volumetric strains are calculated using the mass densities of the reactants and the lithiation products.

Among the binary metal oxides, $MoO_3$ exhibits high theoretical capacity (1117 mA h $g^{-1}$) despite its relatively high formula weight. The capacity surpasses the values of most of transition metal oxides. Indeed, prior studies indicate that such capacity can be achieved in the first cycle of $MoO_3$ [16,17]. Nanoelectrodes of different geometrical shapes were assessed, with different degrees of success, including porous films, nanoparticles, nanobelt films, and nanorods [17–24]. The orthorhombic $MoO_3$ (α-$MoO_3$), composed of layers of distorted $MoO_6$ octahedra, is the thermodynamically stable phase among various polymorphs, and is of general interest in electrochemical applications given its intrinsic layered crystalline structure and the ease of multivalent-state (Mo (VI)/Mo(V)) coupling. It is noteworthy that the reaction mechanism of first delithiation in $MoO_3$ was revealed in great detail in a very recent publication [25]. This paper aims to illustrate the two-step lithiation mechanism and phase evolution in cyclic lithiation of α-$MoO_3$. In comparison to most metal oxides that the high capacity is largely offset by the mechanical degradation [26–29], $MoO_3$ remains defects free in the lithiation cycles in spite of the 90% volumetric change associated with the electrochemical processes. The study is carried out through coordinated *in-situ* transmission electron microcopy (TEM) experiments on α-$MoO_3$ nanobelts and first-principles computational studies based on density functional theories (DFT). The approaches are highly complementary in that the *in-situ* TEM diagnosis provides direct visualization of the real-time electrochemical process while first-principles modeling offer fundamental understanding of the intrinsic behaviors at the electronic/atomic level.

We find that lithiation of α-$MoO_3$ proceeds in two steps: Li intercalation in the early stage lithiation leads to the formation of crystalline $Li_2MoO_3$, and further Li insertion converts $Li_xMoO_3$ to metallic Mo and amorphous $Li_2O$. Li intercalation is due to the occupation of Li at the favorable interstitial sites in the layered structure. This process is thermodynamically more favorable and is accompanied with small deformation of $MoO_3$. The subsequent conversion reaction becomes the rate-limiting step because of the saturation of Li insertion at the well-defined interstitial positions and it induces solid-state amorphization and large volumetric expansion. In the first delithiation, the mixture of Mo and $Li_2O$ react to form amorphous $Li_2MoO_3$. The subsequent cycles ends with Mo and $Li_2O$ upon complete lithiation and $Li_2MoO_3$ as the delithiated products. The combinatory *in-situ* TEM observations and atomistic modeling draw a complete picture of the reaction pathways of α-$MoO_3$ in the lithiation cycles. More interestingly, $MoO_3$ remains free of mechanical defects of dislocations or cracks which are common adverse effects in high-capacity electrodes. The *in-situ* bending experiments demonstrate that lithiation of α-$MoO_3$ transforms a brittle material in the pure form to a material sustainable of large deformation in the lithiated phase. Such a behavior might be the most desirable character in the development of high-performance electrodes of superior mechanical reliability.

## 2. Experimental section

### 2.1. Material synthesis

The synthesis of α-$MoO_3$ nanobelts is based on a modified hydrothermal method [30]. All solvents and chemicals were of reagent quality and were used without further purification. Nitric acid ($HNO_3$), ammonium heptamolybdate tetrahydrate [$(NH_4)_6Mo_7O_{24}\cdot 4H_2O$] were obtained from Beijing Chemical Reagent Co. In a typical synthesis, 1.0 g of [$(NH_4)_6Mo_7O_{24}\cdot 4H_2O$] was dissolved in a mixed solution (36 mL) of 65% $HNO_3$ and deionized $H_2O$ with a corresponding volume ratio of 1:5. After fully dissolved, this reaction solution was transferred into a Teflon-lined stainless steel autoclave (50 mL capacity) and heated at 180 °C in an electric oven for 24 h. After cooling, the white product was collected by centrifugation and washed thoroughly with water and ethanol before drying at 60 °C for 3 h.

### 2.2. Characterization of $MoO_3$ nanobelts by SEM, XRD, TEM, and EELS

The synthesized products were characterized by a scanning electron microscope (FEI-Quanta 250), X-ray diffractometer (XRD, Bruker D8 Advance) equipped with Cu Kα radiation, transmission electron microscopy (TEM, FEI TECHNAI G20, operated at 200 kV), and field emission transmission electron microscopy (FETEM, JEOL-2010F, operated at 200 kV). The chemical composition and valance state of the samples was detected electron energy loss spectroscopy (EELS), the energy resolution of the EELS system is about 1.2 eV.

### 2.3. In-situ experiments

The *in situ* TEM observations were carried out using the Nanofactory TEM-scanning tunneling microscopy (STM) holder inside a JEOL-2010F TEM. A few $MoO_3$ nanobelts were attached to a gold (Au) rod with conductive silver epoxy as the anode. Li metal was scratched by an electrochemically shaped tungsten (W) tip inside a glove box. The Au and W wires were mounted on the station of TEM-STM holder. The assembly holder was loaded into the TEM chamber within a sealed plastic bag with an air exposure time less than 5 s. By manipulating the pizeo-driven stage with nanometer precision on the TEM-STM holder, the $Li_2O$ covered Li metal electrode came into contact with the single $MoO_3$ nanobelt. Once a reliable contact was made, a negative (−3 V) or positive voltage bias (+ 4 V) was applied to drive the lithiation and delithiation reaction of the $MoO_3$ nanobelt.

### 2.4. Half-cell electrochemical measurements

Half-cell electrochemical experiments were performed at a CT2001A Land battery tester at room temperature. To prepare the electrode, slurry was made by mixing the active material, acetylene black, and polyvinylidenefluoride (PVDF) in a weight ratio of 80:10:10 in N-methyl pyrrolidone (NMP) with sonication for 1 h. The working electrodes were made by pasting onto stainless steel foil and drying at 120 °C in vacuum overnight. The electrolyte solution was 1 M $LiPF_6$ dissolved in ethylene carbonate (EC)/dimethyl carbonate (DMC) (1:1 vol ratio). Pure Li foil (Aldrich) was used as the counter electrode. The cells were charged and discharged between 0.001 and 3 V (*vs* $Li/Li^+$) at a current density of 100 mA/g.

## 3. Results and discussion

The diffraction peaks in the powder X-ray diffraction (XRD) pattern (Supporting information Fig. S1a) perfectly match the standard spectrum of α-$MoO_3$ (JFPDF: 05–0508). A large number of the nanobelts are long and straight with the thickness in between 60 and 90 nm, width 200–500 nm, and length 5–10 μm (Supporting information Fig. S1b-d). The TEM image (Fig. 2a) shows the morphology of individual nanobelts. The selected area electron diffraction (SAED) pattern (Fig. 2b) indicates that the growth direction is [001] and the thickness is aligned on the [010] direction. The high-resolution TEM (HRTEM) image in Fig. 2c reveals the single crystallinity of the nanobelts. The cross-section view and the corresponding HRTEM image are shown in Fig. 2d and e.

We integrate a single α-$MoO_3$ nanobelt into a solid-state nanobattery setup and perform *in-situ* electrochemical experiments of lithiation/delithiation [31,32]. Fig. 3(a) shows the schematic of the experimental setup, consisting of an α-$MoO_3$ nanobelt as the working electrode, $Li/Li_2O$ as the counter electrode and the electrolyte, and Au and W rods as the current collectors. Lithiation and delithiation are carried out by applying a bias voltage of −3 V and +4 V between the α-$MoO_3$ nanobelt and the Li counter electrode.

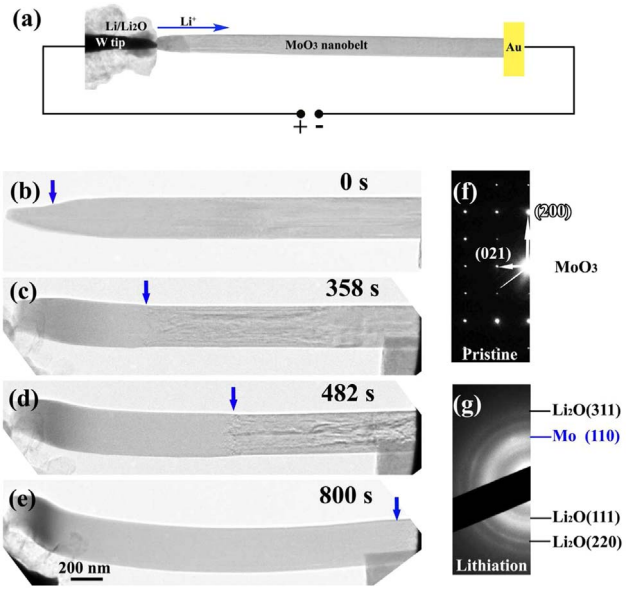


**Fig. 3.** (a) Schematic of a solid-state nanobattery in TEM consisting of a $MoO_3$ nanobelt as the working electrode, $Li/Li_2O$ as the counter electrode and the electrolyte. The Au and W rods are current collectors. (b–e) In-situ visualization of lithiation of the $MoO_3$ nanobelt. The blue arrows indicate the location of the reaction front. The lithiated phase remains defects free in spite of volume expansion of $MoO_3$ during lithiation. (f, g) SAED patterns of the pristine $MoO_3$ and its fully lithiated state indicate that $MoO_3$ transforms to metallic Mo and amorphous $Li_2O$ upon complete lithiation.

A large voltage is necessary to drive the electrochemical reactions because of the small size and poor electronic conductivity of the nanobelt. Precautions were taken to avoid the beam effects on lithiation reactions. The *in-situ* experiments are carried out with a low dose rate of electron flux. During the entire experiments, the electron beam is distributed to a large illumination area with the diameter of 50 μm. We avoid the focus of beams to a small area that may induce undesired radiation effects. Fig. 3b–e and Supporting information Movie S1 show the propagation of the

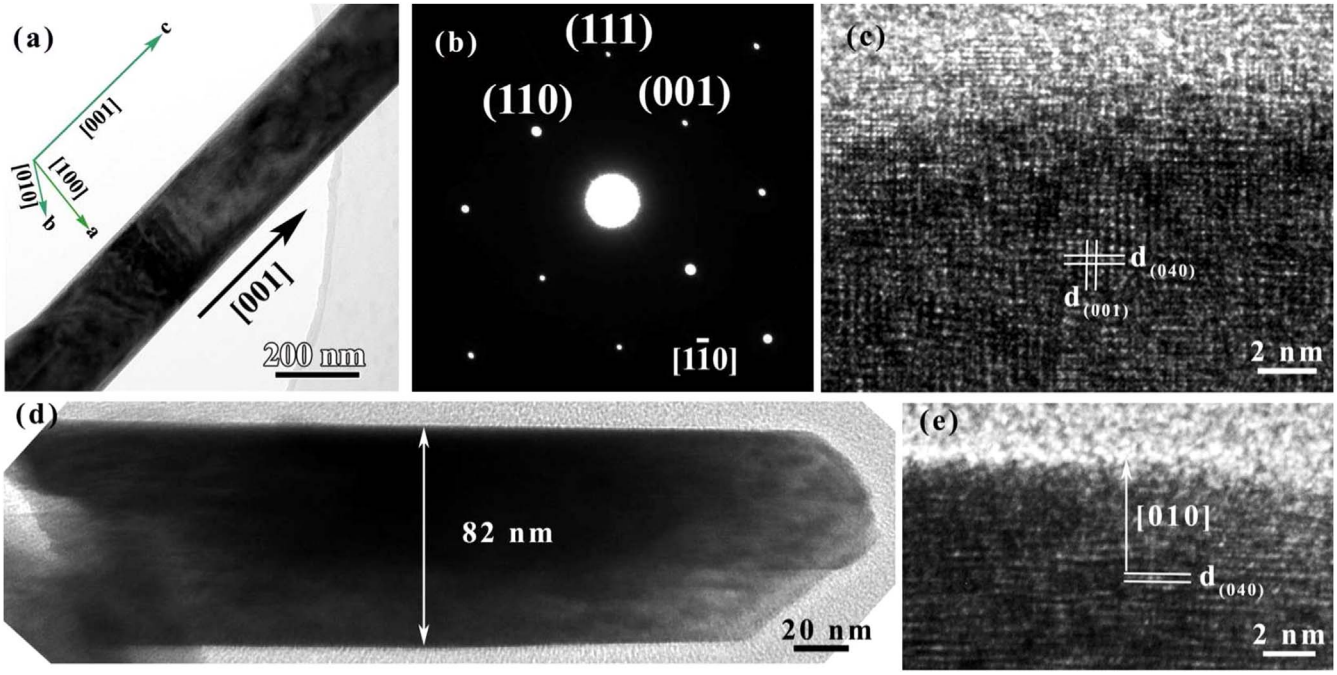


**Fig. 2.** Microstructure characterization of as-prepared α-$MoO_3$ nanobelts. (a) Magnified TEM image and (b) SAED pattern of a single $MoO_3$ nanobelt, (c) HRTEM image of $MoO_3$ nanobelt showing the single crystalline feature and lattice fringes. (d, e) Cross section view and the corresponding HRTEM image.

reaction front and the morphological evolution of the α-$MoO_3$ nanobelt in the first lithiation. Here the location of the reaction front, indicated by the blue arrows, is marked as the boundary which separates the swelled lithiated part and the undeformed pristine phase. It appears that no apparent dislocation clouds present at the reaction front as was observed in $SnO_2$ nanowires [33] or cracks reported for ZnO and $RuO_2$ nanowires [34,35]. The ripples ahead of the reaction front are likely due to the rotational contrast in the TEM images. The surface of the nanobelt after full lithiation remains very smooth. Fig. 3f-g shows the SAED patterns of the pristine $MoO_3$ and its fully lithiated state. The clear diffraction spots at the initial state are attributed to the single crystalline α-$MoO_3$. Upon complete lithiation, it shows a mixture of Mo nanograins and amorphous $Li_2O$ with an overall polycrystalline nature. The diffuse ring can be indexed to Mo (110) indicating the ultrafine feature of Mo crystals, and (111), (220), and (311) plane of cubic $Li_2O$ phase are also present. The electron energy loss spectroscopy (EELS) spectrum of Li-K edge (~60 eV) in Supporting Information Fig. S2 is similar to that of $Li_2O$ which further confirms the lithiation reaction.

We examine the lithiation mechanism of α-$MoO_3$ more closely by identifying the phase evolution along the reaction pathway. It is interesting that $MoO_3$ experiences two-step lithiation which is a distinct feature from the typical insertion or conversion mechanism. The dynamic evolution is recorded in the Supporting information Movie S2. In the early stage of lithiation, Li intercalation in the layered structure leads to the formation of crystalline $Li_2MoO_3$. With further Li insertion, $Li_xMoO_3$ is converted to metallic Mo and amorphous $Li_2O$. Fig. 4a marks the three domains representing the fully lithiated state, intermediate $Li_2MoO_3$ phase, and pristine $MoO_3$ along the lithiation direction. Fig. 4b shows the corresponding SAED patterns in the three domains. Overall, we see a transition from an amorphous matrix containing polycrystalline phases to the single crystalline zone along the path. The clear diffraction pattern for the intermediate $Li_2MoO_3$ phase indicates that the crystalline structure of $MoO_3$ is well retained during the first-step lithiation. Further lithiation distorts and amorphizes the lattice leading to the formation of ultrafine Mo clusters dispersed in the $Li_2O$ matrix. Such a behavior may stem from the intrinsic layered structure of α-$MoO_3$ – the intercalation behavior is a reminiscence of lithiation of typical layered structure of cathodes, while the conversion reaction occurs in a similar way in the conversion-type binary metal oxides. Fig. 4c shows the schematic of phase evolution and snapshots at different lithiation stages. Fig. 4d plots the area growth rate as a function of the lithiation time. The dimensional change in the thickness direction is difficult to measure in the TEM experiments. The area growth rate of the $MoO_3$ nanobelt further delineates the two-step lithiation behavior. Li interaction is accompanied with a small areal expansion (~2.3%) and occurs at a fast rate (~28 s). In comparison, the conversion reaction is kinetically slow which consumes the majority of lithiation time. This process also causes a significantly larger swelling of the nanobelt (~30% areal growth) with a nearly constant expansion rate. The dynamic behavior in the two steps indicates that the intercalation process is thermodynamically more favorable in α-$MoO_3$ while the conversion reaction is the kinetically limiting step for the overall lithiation.

The two-step lithiation mechanism was observed in previous

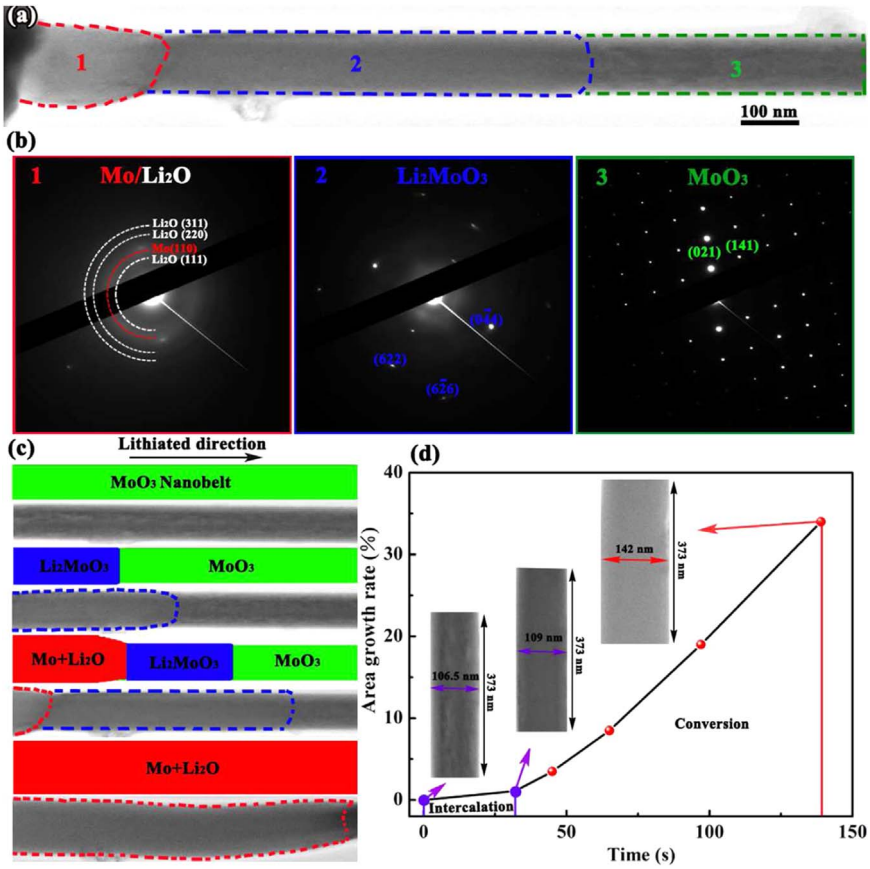


**Fig. 4.** Two-step lithiation of α-$MoO_3$ – Li intercalation leads to the formation of crystalline $Li_2MoO_3$ in the early stage of lithiation, and further Li insertion coverts $Li_xMoO_3$ to Mo nanograins and amorphous $Li_2O$. (a) The three domains represent the fully lithiated state, intermediate $Li_2MoO_3$ phase, and pristine $MoO_3$. (b) SAED patterns in the three domains. (c) Schematic of the reaction path and respective TEM images. (d)The area growth rate of the $MoO_3$ nanobelt further delineates the two-step lithiation. Li interaction occurs at a fast rate and is accompanied with a small areal expansion. In comparison, the conversion reaction is kinetically slow and causes a large swelling of the nanobelt.

electrochemical measurements [23]. We also perform galvanostatic experiments to correlate the macroscopic electrochemical performance with the microscopic observations. Supporting Information Fig. S3 shows the first cycle curve. The first lithiation clearly shows two regions: the region above 1.5 V (region I) with two plateaus at 2.7 V and 2.3 V corresponds to the process of Li intercalation, and the region below 1.5 V (region II) represents the stage that the conversion reaction proceeds with a long plateau around 0.4 V. In the first delithiation, the two plateaus around 2.7 V and 2.3 V are indiscernible, indicating that the intercalation process is irreversible which results in a low Columbic efficiency (~43%) in the first cycle. It is evident that the material behaviors in the electrochemical tests and in the TEM setup utilizing a single nano-battery are closely correlated, while the *in-situ* TEM experiments provides the unprecedented resolution on the microscopic events that govern the large-scale performance.

We perform first-principles theoretical studies to attain full understanding of the microscopic mechanism of lithiation in α-$MoO_3$. Projector-augmented-wave (PAW) potentials in Vienna Ab-initio Simulation Package (VASP) are used to mimic the ionic cores, while the generalized gradient approximation (GGA) in the Perdew-Burke-Ernzerhof (PBE) flavor is employed for the exchange and correlation functional [36,37]. The Hubbard U-J parameter 6.3 for Mo is adopted to model the large Coulombic repulsion between localized electrons [38]. The atomic structures and system energy are calculated with an energy cutoff of 520 eV. For Brillouin zone sampling, a $5\times3\times5$ mesh of $k$ points in the Monkhorst-Pack scheme is sufficient in the energetic relaxation of $Li_xMoO_3$. The energy optimization is considered complete when the magnitude of the force on each atom is smaller than 0.02 eV $Å^{-1}$. In addition, the DFT-D2 method is used with a global scaling factor of 0.75 for correction of the van der Waals interaction between interlayers in α-$MoO_3$ [39]. The unit cell of α-$MoO_3$ has the space group of *Pbnm* and contains 16 atoms. The lattice parameters for the unit cell are $a=3.83$ Å, $b=13.89$ Å, and $c=3.73$ Å, which are very close to the experimental values [40].

We first examine the energetics and structural features during Li insertion into α-$MoO_3$. We incrementally increase Li concentration to model the lithiation process. We consider five possible configurations of $Li_xMoO_3$ at a given Li concentration with different Li distributions in each, to eliminate the large variations inherent to the small model size. At each Li concentration, we perform the Delaunay triangulation analysis to identify the possible favorite sites for Li insertion [41]. The formation energy per Li is defined as $E_f(n) = [E_{nLi-MoO_3} - E_{MoO_3} - nE_{Li}]/n$. Here the energy of $MoO_3$ ($E_{MoO3}$) and the energy of a Li atom in its bulk form ($E_{Li}$) are taken as the reference energies and $E_{nLi\text{-}MoO3}$ is the total energy of the system containing $n$ Li atoms in the cell. We identify two favorable interstitial positions (Fig. 5a) for Li intercalation – the interlayer and intralayer sites with formation energies of −3.57 eV and −3.68 eV, respectively. The interlayer site is surrounded by four terminal O1 atoms and one O2 atom in the adjacent layer, while the intralayer site is neighbored with two O2 atoms and two O3 atoms [42]. The energy barrier of Li diffusion along the

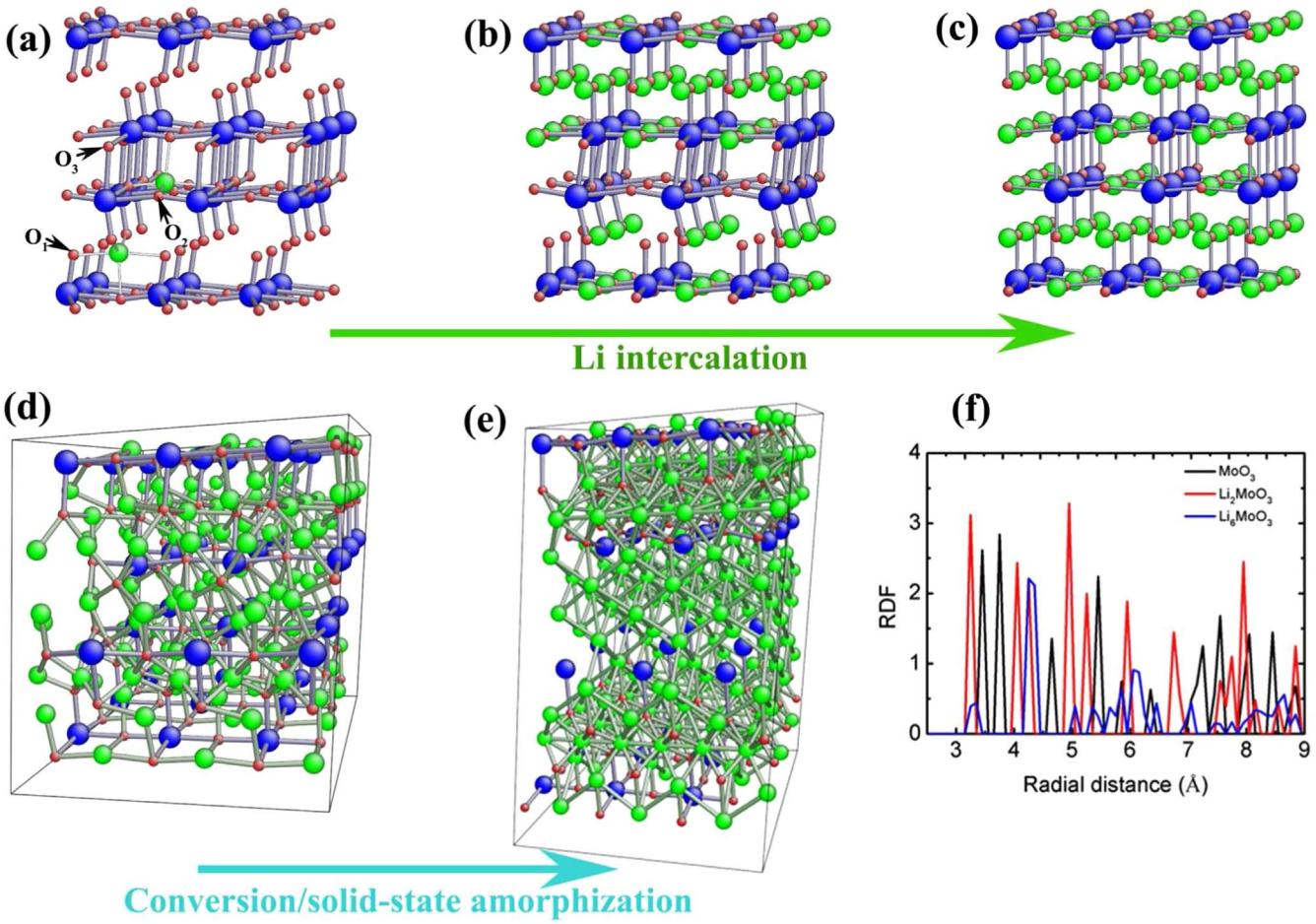


**Fig. 5.** First-principles modeling on the two-step lithiation of α-$MoO_3$. (a) The interlayer and intralayer sites are the two favorable interstitial positions for Li intercalation in α-$MoO_3$. (b, c) Li occupies the favorable interstitial sites which induces the formation of crystalline $Li_2MO_3$. (d, e) The conversion reaction causes solid-state amorphization of the structure. (f) RDF plot of the Mo-Mo pairs in $MoO_3$, $Li_2MoO_3$ and $Li_6MoO_3$. The compositions in (b)-(e) are $Li_{1.5}MoO_3$, $Li_2MoO_3$, $Li_{3.75}MoO_3$, and $Li_6MoO_3$, respectively. The atomic configurations are expanded views consisting of $3\times1\times3$ unit cells. The blue, red, and green spheres represent Mo, O, and Li atoms.

interlayer-intralayer pathway is calculated as 0.55 eV (Supporting information Fig. S4) that is consistent with the previous study [43]. The unit cell contains a total number of 8 interlayer and intralayer sites for Li intercalation. Those interstitial spots are filled by Li at the early stage of lithiation. Additional Li are placed at the sites of largest Delaunay triangular volume which are regarded as generally favorable sites for Li insertion. In each step, 1 Li is added into the lattice to model the composition range $0.25 \leq x \leq 6$ in $Li_xMoO_3$. Fig. 5b–e shows the geometry at four representative Li concentrations, $Li_{1.5}MoO_3$, $Li_2MoO_3$, $Li_{3.75}MoO_3$, and $Li_6MoO_3$, respectively. The layered structure is well maintained up to the composition $Li_2MoO_3$. Beyond this point, Li insertion breaks the Mo–O bonds and induces solid-state amorphization of the structure. The radial distribution function (RDF) is plotted (Fig. 5f) for the pristine $MoO_3$, $Li_2MoO_3$, and fully lithiated state $Li_6MoO_3$ to show the transition from the layered crystalline structure to the eventual amorphous state.

Fig. 6a shows the evolution of the formation energy and strains as a function of the Li concentration. The solid symbols represent the average values from the five different configurations for each given composition, and error bars represents the standard deviation. The variation of formation energy clearly demonstrates the two-stage lithiation mechanism. Up to the composition $Li_2MoO_3$, the formation energy remains a nearly constant value of $-3.6$ eV. Li intercalation at the interlay and intralayer sites is highly favorable with a large thermodynamic driving force. In the next stage from $Li_2MoO_3$ to $Li_6MoO_3$, the formation energy decreases rapidly (more positive) as the Li concentration increases due to the saturation of the intercalation sites and growing repulsion between the neighboring Li atoms. Such a behavior is also seen in the plot of evolution of volumetric strains in Fig. 6b. As expected, the intercalation process is accompanied with minor volumetric deformation and the crystalline structure is well retained. The volumetric strain increases dramatically afterwards and reaches ~90% upon complete lithiation. The large volumetric deformation is accommodated by the gradual rearrangement of the lattice structure through Mo–O bond breaking and Li-Mo-O cluster reforming as shown in Fig. 5. It is also worth noting that the deformation of $MoO_3$ during lithiation is anisotropic. The in-plane strain ($\varepsilon_x$) along the *a*-axis and out-of-plane strain along the *b*-axis ($\varepsilon_y$) are included in Fig. 6b. The deformation in the in-plane directions is relatively small. The decrease of lattice length in the *b*-axis (negative $\varepsilon_y$) in the intercalation process is due to the attraction between the oxygen layers with Li. The evolution of the formation energy and strains in the modeling agree well with the TEM observations (Fig. 4d) on the kinetics and deformation of α-$MoO_3$ during lithiation.

We assess the microstructure evolution of $MoO_3$ in the lithiation and delithiation cycles by *in-situ* TEM experiments. Fig. 7a shows the pristine α-$MoO_3$ nanobelt. As discussed, $MoO_3$ experiences Li intercalation and then conversion reaction in the first lithiation process. The diffuse rings in Fig. 7b demonstrate the generation of ultrafine Mo nanoclusters embedded in a $Li_2O$ matrix. The width of the nanobelt increases from 176 nm to 202.5 nm. As pointed out earlier, a recent paper studied the delithiation mechanism of $MoO_3$ [25]. Our experiments showed the same delithiation behavior so we will not repeat those interesting findings. In brief, the mixture of Mo nanograins and $Li_2O$ react to form intermediate crystalline $Li_{1.66}Mo_{0.66}O_3$ and then amorphous $Li_2MoO_3$ upon complete delithiation [25]. The electrochemical reactivity of $Li_2O$ was attributed to the electrocatalytic effect of Mo nanograins dispersed in the $Li_2O$ matrix. The SAED pattern confirms the formation of $Li_2MoO_3$ after delithiation. The width of the nanobelt decreases to 178 nm that is comparable to width of the pristine material. The irreversible phase change in the first lithiation cycle dictates the capacity fading – 1/3 of the theoretical capacity is lost due to the irreversible conversion reactions. The reaction products in the second lithiation cycles are shown in Fig. 7c-d. The SAED patterns show that Mo/$Li_2O$ form after the second lithiation and $Li_2MoO_3$ again is generated after the second delithiation. Such phase evolution is reversible in the subsequent cycles. In summary, the first lithiation proceeds with $MoO_3 + 2e^- + 2Li^+ \rightarrow Li_2MoO_3$ during Li intercalation and $Li_2MoO_3 + 4e^- + 4Li^+ \rightarrow Mo + 3Li_2O$ during the conversion reaction. The subsequent cycles follow the reaction of $Li_2MoO_3 + 4e^- + 4Li^+ \leftrightarrow Mo + 3Li_2O$. Such reaction mechanisms may explain the low columbic efficiency commonly observed in the first cycle of $MoO_3$ while the capacity can be well retained in the subsequent cycles.

In addition to the direct observation of the reaction mechanism, Fig. 7 is also a clear demonstration of the mechanical robustness of the $MoO_3$ nanobelts in the lithiation cycles. Despite the large repetitive volumetric change, the nanobelts do not form any mechanical defects such as profuse dislocation clouds or cracks as typically observed in other metal oxides. Furthermore, the size change of the nanobelt in the multiple cycles is irreversible which is beneficial for the maintenance of structural integrity of composite electrodes in long-term cycles. We perform *in-situ* bending experiments on a pristine $MoO_3$ nanobelt and its fully lithiated state to characterize the mechanical behaviors. Lithiation usually results in dramatic changes of the mechanical properties of

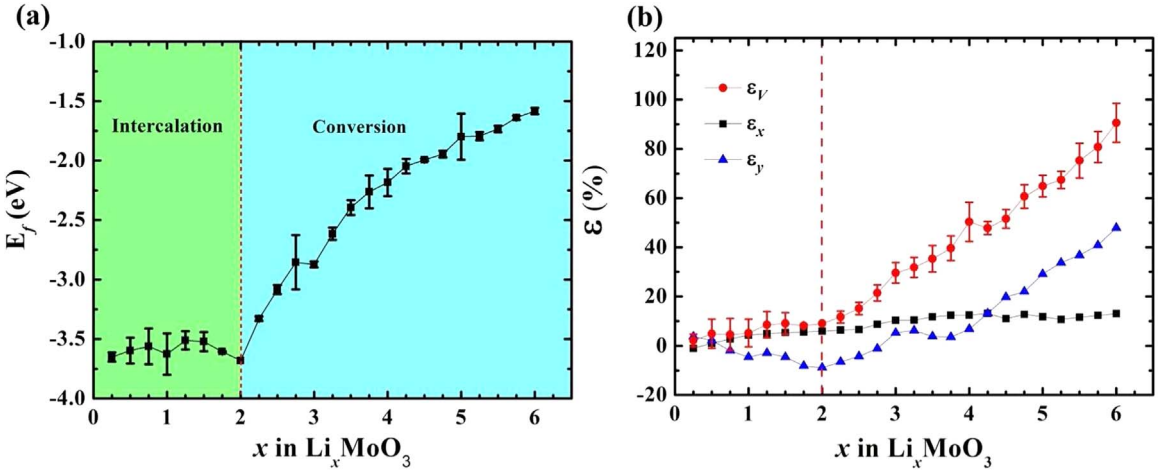


**Fig. 6.** The two-step lithiation of $MoO_3$ evident in (a) the formation energy per Li in $Li_xMoO3$ and (b) strains in the in-plan ($\varepsilon_x$) direction, out-of-plan ($\varepsilon_y$) direction, and the total volumetric strain ($\varepsilon_v$). The solid symbols represent the average values of the formation energy per Li or strains from five different configurations of $Li_xMoO_3$, and error bars represents the standard deviation.

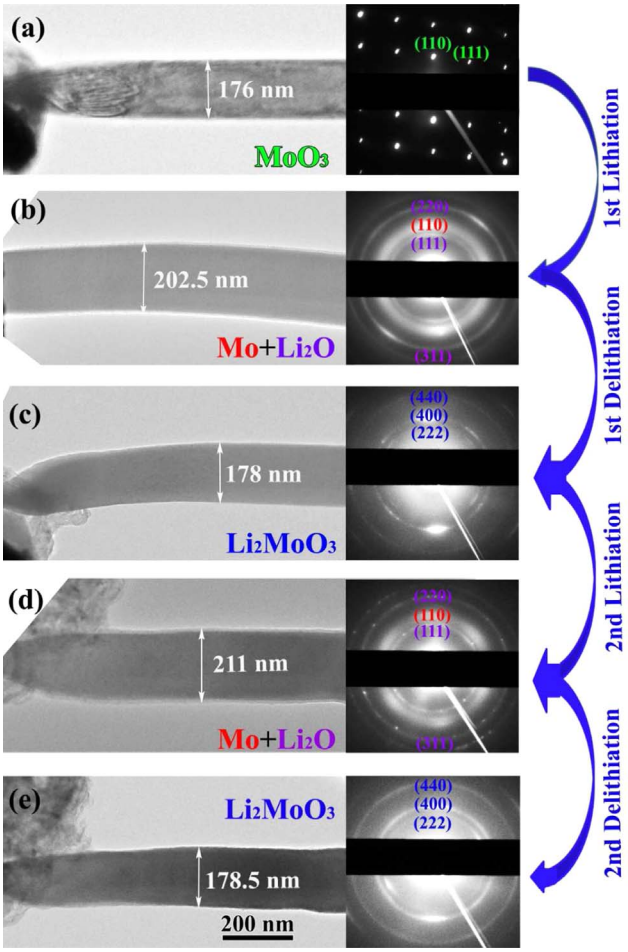


**Fig. 7.** The microstructure evolution of $MoO_3$ nanobelt in the first two lithiation/delithiation cycles. The first lithiation converts $MoO_3$ into Mo nanograins and amorphous $Li_2O$. The mixture of Mo and $Li_2O$ react and form amorphous $Li_2MoO_3$ upon the first delithiation. The subsequent cycles ends with Mo and $Li_2O$ as the lithiation products and $Li_2MoO_3$ as the delithiated compound.

electrodes due to the compositional change [44]. Fig. 8a-d and Supporting information Movie S3 show the snapshots of the pristine nanobelt during bending deformation. The nanobelt can fully recover its initial shape up to the bending strain ~4%, and it breaks beyond this load. In comparison, large bending strain can be sustained in lithiated $MoO_3$ nanobelts as shown in Fig. 8e-h and Supporting information Movie S4. The maximum local strain reaches ~11% without causing any cracks. This behavior differs from the Li-embrittlement (a similar phenomenon of hydrogen embrittlement) [45] observed in lithiated ZnO and $RuO_2$ [34,35]. After unloading, the morphology of the nanobelt cannot fully recover to its original stage. The durable nature of lithiated $MoO_3$ may originate from the flowability that accommodates the large deformation in the electrochemical process of lithiation and delithiation [46]. The mechanical resilience of $MoO_3$ may be attributed to the aliovalency of the Mo cation; the valence states of Mo (IV), Mo(V), and Mo(VI) can be easily translated. Therefore, when Li are inserted to reduce the original cation, Mo can gradually adapt to the electronic and structural changes instead of experiencing sharp cleavage of Mo–O bonds. The flowability of lithiated $MoO_3$ may also benefit from the softness of $Li_2O$ matrix [47] in contrast to the brittleness of the original $MoO_3$ crystalline structure.

## 4. Conclusion

In conclusion, we systematically study the reaction mechanism, structural evolution, and mechanical stability of α-$MoO_3$ through complementary *in-situ* TEM experiments and first-principles modeling. The chemistry of Li and $MoO_3$ differs from that of typical insertion- or conversion-type binary metal oxides. The first lithiation proceeds with two-stage reactions; Li intercalation in the early stage stems from the layered structure of α-$MoO_3$. Such a process is thermodynamically more favorable and is accompanied with a minor volumetric change. Further Li insertion beyond $Li_2MoO_3$ leads to the solid-state amorphization and conversion to the mixture of Mo nanograins and $Li_2O$ matrix. The conversion reaction is the rate-limiting step for the charge kinetics and induces large deformation. The *in-situ* TEM experiments depict the complete reaction pathway of $MoO_3$ in the cycles of lithiation and delithiation. Despite the large cyclic deformation that is a common feature inherent to high-capacity electrodes, $MoO_3$ shows unprecedented mechanical reliability. The fundamental studies on the electro-chemo-mechanical behaviors of $MoO_3$ shed insight on the development of durable high-capacity electrodes of improved electrochemical and mechanical stabilities.

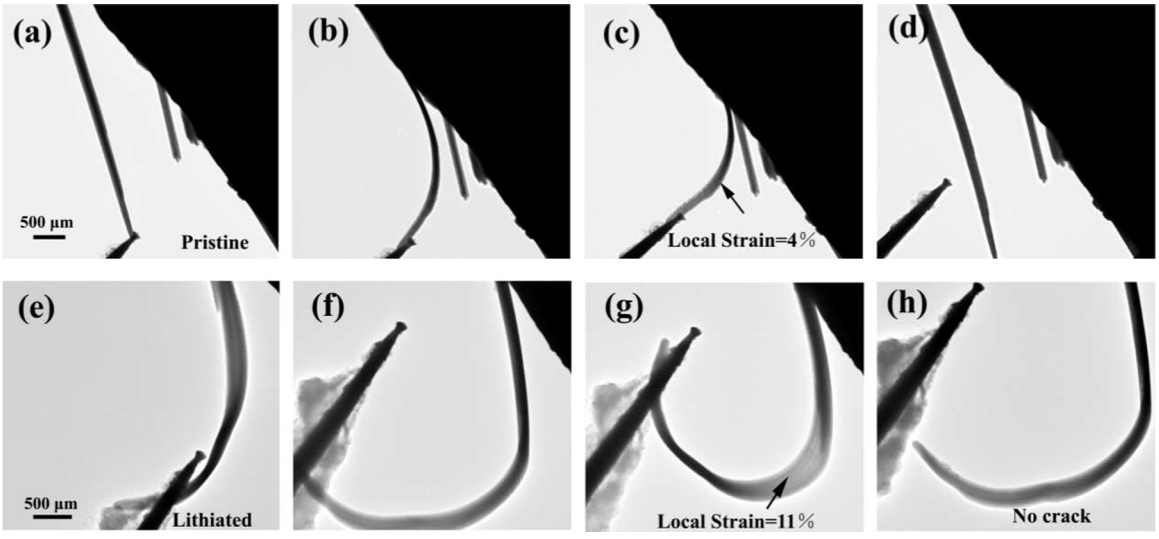


**Fig. 8.** In-situ bending experiments of (a-d) a pristine $MoO_3$ nanobelt and (e-h) lithiated $MoO_3$ nanobelt. Pristine $MoO_3$ is brittle, while lithiated $MoO_3$ exhibits large plasticity and crack-free when the applied bending strain reaches 11%.

## Acknowledgments

K.Z. is grateful for the support of the National Science Foundation through the grant CBET-1603866. Y.Z. acknowledges the Beijing Municipal Natural Science Foundation (2132014) and Special Projects for Development of National Major Scientific Instruments and Equipment (2012YQ03007508).

## Appendix A. Supplementary information

Supplementary data associated with this article can be found in the online version at http://dx.doi.org/10.1016/j.nanoen.2016.06.045.

## References

[1] R.F. Service, Science 344 (2014) 352–354.
[2] R. Van Noorden, Nature 507 (2014) 26–28.
[3] J.M. Tarascon, M. Armand, Nature 414 (2001) 359–367.
[4] M. Reddy, G. Subba Rao, B. Chowdari, Chem. Rev. 113 (2013) 5364–5457.
[5] J. Cabana, L. Monconduit, D. Larcher, M.R. Palacin, Adv. Mater. 22 (2010) E170–E192.
[6] Y. Tang, Y. Zhang, J. Deng, J. Wei, H.L. Tam, B.K. Chandran, Z. Dong, Z. Chen, X. Chen, Adv. Mater. 26 (2014) 6111–6118.
[7] S. Liu, Z. Wang, C. Yu, H.B. Wu, G. Wang, Q. Dong, J. Qiu, A. Eychmüller, A Adv. Mater. 25 (2013) 3462–3467.
[8] N.A. Chernova, M. Roppolo, A.C. Dillon, M.S. Whittingham, J. Mater. Chem. 19 (2009) 2526–2552.
[9] L. Mai, L. Xu, C. Han, X. Xu, Y. Luo, S. Zhao, Y. Zhao, Nano Lett. 10 (2010) 4750–4755.
[10] Y. Li, B. Tan, Y. Wu, Nano Lett. 8 (2008) 265–270.
[11] X.W. Lou, D. Deng, J.Y. Lee, J. Feng, L.A. Archer, Adv. Mater. 20 (2008) 258–262.
[12] X. Gao, J. Bao, G. Pan, H. Zhu, P. Huang, F. Wu, D. Song, J. Phys. Chem. B 108 (2004) 5547–5551.
[13] X. Zhu, Y. Zhu, S. Murali, M.D. Stoller, R.S. Ruoff, ACS Nano 5 (2011) 3333–3338.
[14] B. Varghese, M. Reddy, Z. Yanwu, C.S. Lit, T.C. Hoong, G. Subba Rao, B. Chowdari, A. T.S. Wee, C.T. Lim, C.-H. Sow, Chem. Mater. 20 (2008) 3360–3367.
[15] K. He, H.L. Xin, K. Zhao, X. Yu, D. Nordlund, T.-C. Weng, J. Li, Y. Jiang, C. A. Cadigan, R.M. Richards, Nano Lett. 15 (2015) 1437–1444.
[16] S.H. Lee, Y.H. Kim, R. Deshpande, P.A. Parilla, E. Whitney, D.T. Gillaspie, K. M. Jones, A. Mahan, S. Zhang, A.C. Dillon, Adv. Mater. 20 (2008) 3627–3632.
[17] Y.S. Jung, S. Lee, D. Ahn, A.C. Dillon, S.-H. Lee, J. Power Sources 188 (2009) 286–291.
[18] L.A. Riley, S.-H. Lee, L. Gedvilias, A.C. Dillon, J. Power Sources 195 (2010) 588–592.
[19] M.F. Hassan, Z. Guo, Z. Chen, H. Liu, J. Power Sources 195 (2010) 2372–2376.
[20] G. Zhao, N. Zhang, K. Sun, J. Mater. Chem. A 1 (2013) 221–224.
[21] Q. Wang, J. Sun, Q. Wang, D.-a Zhang, L. Xing, X. Xue, J. Mater. Chem. A 3 (2015) 5083–5091.
[22] Q. Xia, H. Zhao, Z. Du, J. Wang, T. Zhang, J. Wang, P. Lv, J. Power Sources 226 (2013) 107–111.
[23] Y. Sun, J. Wang, B. Zhao, R. Cai, R. Ran, Z. Shao, J. Mater. Chem. A 1 (2013) 4736–4746.
[24] C.-L. Liu, Y. Wang, C. Zhang, X.-S. Li, W.-S. Dong, Mater. Chem. Phys. 143 (2014) 1111–1118.
[25] W. Xia, Q. Zhang, F. Xu, L. Sun, ACS Appl. Mater. Interfaces 8 (2016) 9170–9177.
[26] H. Kim, J.T. Lee, A. Magasinski, K. Zhao, Y. Liu, G. Yushin, Adv. Energy Mater. 5 (2015) 1501306.
[27] M.T. McDowell, S.W. Lee, I. Ryu, H. Wu, W.D. Nix, J.W. Choi, Y. Cui, Nano Lett. 11 (2011) 4018–4025.
[28] C.K. Chan, X.F. Zhang, Y. Cui, Nano Lett. 8 (2008) 307–309.
[29] R. Xu, K. Zhao, Extrem. Mech. Lett. (2015), http://dx.doi.org/10.1016/j.eml.2015.10.004.
[30] Z. Wang, S. Madhavi, X.W. Lou, J. Phys. Chem. C 116 (2012) 12508–12513.
[31] Y. Zhang, Y. Li, Z. Wang, K. Zhao, Nano Lett. 14 (2014) 7161–7170.
[32] Y. Zhang, Z. Wang, Y. Li, K. Zhao, Mech. Mater. 91 (2015) 313–322.
[33] J.Y. Huang, L. Zhong, C.M. Wang, J.P. Sullivan, W. Xu, L.Q. Zhang, S.X. Mao, N. S. Hudak, X.H. Liu, A. Subramanian, H.Y. Fan, L.A. Qi, A. Kushima, J. Li, Science 330 (2010) 1515–1520.
[34] A. Kushima, X.H. Liu, G. Zhu, Z.L. Wang, J.Y. Huang, J. Li, Nano Lett. 11 (2011) 4535–4541.
[35] K.E. Gregorczyk, Y. Liu, J.P. Sullivan, G.W. Rubloff, ACS Nano 7 (2013) 6354–6360.
[36] G. Kresse, J. Furthmüller, Phys. Rev. B 54 (1996) 11169.
[37] G. Kresse, D. Joubert, Phys. Rev. B 59 (1999) 1758.
[38] R. Coquet, D.J. Willock, Phys. Chem. Chem. Phys. 7 (2005) 3819–3828.
[39] H. Ding, K.G. Ray, V. Ozolins, M. Asta, Phys. Rev. B 85 (2012) 012104.
[40] H. Sitepu, B.H. O'Connor, D. Li, J. Appl. Cryst. 38 (2005) 158–167.
[41] K.J. Zhao, G.A. Tritsaris, M. Pharr, W.L. Wang, O. Okeke, Z.G. Suo, J.J. Vlassak, E. Kaxiras, Nano Lett. 12 (2012) 4397–4403.
[42] M. Baldoni, L. Craco, G. Seifert, S. Leoni, J. Mater. Chem. A 1 (2013) 1778–1784.
[43] F. Li, C.R. Cabrera, Z. Chen, J. Mater. Chem. A 2 (2014) 19180–19188.
[44] K.J. Zhao, W.L. Wang, J. Gregoire, M. Pharr, Z.G. Suo, J.J. Vlassak, E. Kaxiras, Nano Lett. 11 (2011) 2962–2967.
[45] Y. Liu, H. Zheng, X.H. Liu, S. Huang, T. Zhu, J. Wang, A. Kushima, N.S. Hudak, X. Huang, S. Zhang, ACS Nano 5 (2011) 7245–7253.
[46] K.J. Zhao, M. Pharr, J.J. Vlassak, Z.G. Suo, J. Appl. Phys. 109 (2011) 016110.
[47] Y. Liu, N.S. Hudak, D.L. Huber, S.J. Limmer, J.P. Sullivan, J.Y. Huang, Nano Lett. 11 (2011) 4188–4194.

**Yonghe Li** is a Ph.D. candidate supervised by Prof. Yuefei Zhang and Prof. Xiaodong Han at the Institute of Microstructure and Property of Advanced Materials, Beijing University of Technology. His research focuses on the *in situ* TEM probing the electro-chemo-mechanics behaviors in high-performance Li/Na-ion batteries and supercapacitors.

**Hong Sun** is a Ph.D. student supervised by Prof. Kejie Zhao at Purdue University. She is interested in atomistic modeling of energy materials.

**Xiaopeng Cheng** is a master student at the Institute of Microstructure and Property of Advanced Materials, Beijing University of Technology supervised by Prof. Yuefei Zhang. His research interest is on atomic layer deposition (ALD) assisted fabrication of nanostructured electrodes materials for LIBs and supercapacitors.

**Yuefei Zhang** received his B.S., M.S. from Taiyuan University of Technology in 1999 and 2002, respectively, and Ph.D. from Beijing University of Technology in 2008 supervised by Prof. Ze Zhang. From 2014 to 2015, he worked as visiting scholar with Prof. Ju Li at MIT. He is now a full professor at the Institute of Microstructure and Property of Advanced Materials, Beijing University of Technology. His research group is focused on the *in situ* TEM/SEM experiments to reveal the microscopic mechanisms that govern the performance of energy storage materials.

**Kejie Zhao** is an Assistant Professor of Mechanical Engineering at Purdue University. He received his Ph.D. degree in Engineering Science in 2012 from Harvard University, and obtained his bachelor's and master's degrees from Xi'an Jiaotong University in China in 2005 and 2008, respectively. He joined the faculty of Purdue University in 2014. His research interests include mechanics of energy materials, high-temperature ceramics, and nanotwinned metals using atomistic modeling and *in-situ* experiments.